Check for updates

Preparation of different phase structure nano sized FePO₄/C cathode material by ultrasonic-assisting and their electrochemical performance†

Chunmei Tang,[a] Wei Ma,[a] Jichuan Huo*[a] and Shuxin Liu [ID] *[b]

As one of the cathode materials for phosphate-based sodium ion batteries, $FePO_4$ has received extensive attention due to its excellent theoretical capacity and stability. However, the $FePO_4$ cathode has the problem of low ionic conductivity and electronic conductivity, which limits its application in sodium-ion batteries. The phase composition and microstructure of $FePO_4$ are crucial to ensure the excellent electrochemical properties. Therefore, in this paper, the nano-sized amorphous $FePO_4 \cdot 2H_2O/C$ with a particle size of only 50 nm was prepared by ultrasonic-assisted precipitation. The carbon black oxidized can be uniformly dispersed in samples and form a spatial network structure. Four kinds of crystalline cathode materials were successfully prepared by further treatment of $FePO_4 \cdot 2H_2O/C$, including amorphous $FePO_4/C$, hexagonal $FePO_4/C$, monoclinic $FePO_4 \cdot 2H_2O/C$ and monoclinic/orthogonal $FePO_4 \cdot 2H_2O/C$. The microstructure, phase composition, particle size distribution and specific surface area of the samples were characterized by XRD, SEM, TEM, EDS, Raman, and BET. The results show that the amorphous $FePO_4/C$ particle size is smaller, and the specific surface area is larger. The electrochemical properties of samples were analyzed by CV and EIS. The results show that the crystal structure affects the specific charge–discharge capacity, Na^+ diffusion coefficient, and charge transfer resistance of the materials. The amorphous $FePO_4/C$ has excellent electrochemical performance, the specific discharge capacity is 149.8 mA h g^{-1}, the Na^+ diffusion coefficient is 2.71 × 10^{-16} cm^2 s^{-1}, and the charge transfer resistance is 139 Ω. The results show that the amorphous structure is effective for improving the electrochemical performance of $FePO_4$ cathode materials.

1 Introduction

Lithium-ion batteries are currently one of the most common rechargeable batteries, and they are widely used in electronic devices, automobiles, power storage and so on. However, due to the limitation of lithium resources, and people's demand for low cost, strong safety, resource sustainability and higher energy density, the research and development of other secondary battery technologies, such as potassium ion batteries, aluminum ion batteries, and sodium-ion batteries, have gradually attracted attention.[1] However, these batteries come with their own set of limitations and challenges. For example, aluminum ion batteries are prone to side reactions during charging and discharging, especially hydrogen evolution reactions, affecting their cycle stability and energy efficiency.[2] Potassium ion batteries face challenges such as volume expansion and slow kinetics, resulting in poor performance during high-rate charge and discharge.[3] And sodium-ion batteries have problems such as poor conductivity.[4] For potassium ion batteries, Zhang *et al.*[5] reported the ternary $Bi_{0.4}Sb_{1.6}Te_3$ nanoparticles coupled with few-layered graphene hybrids, which exhibit a mitigated expansion of 28% during the potassiation/depotassiation process. At the same time, aiming at the problems existing in aluminum ion batteries, Zhang *et al.*[6] designed a deep eutectic electrolyte named HEE30 to significantly improve the reversibility and electrochemical stability of aluminum ion batteries in a wide temperature range of −20 to 60 °C. For sodium-ion batteries, Hu *et al.*[7] designed a series of Nasicon-type $Na_{3+x}MnTi_{1-x}V_x(PO_4)_3$ cathode materials, which have multi-electron reactions, and have a high-voltage platform. Yang *et al.*[8] proposed an interconnected microchip composed of carbon nanotubes and sulfur-doped $TiO_2(CNT/S\text{-}TiO_2)$ as a high-performance anode material for SIBs, enhancing the conductivity and improving the ion transport kinetics. In a word, researchers are constantly exploring the technical improvement and development of various secondary batteries in terms of performance improvement, cost control, material selection and charge–discharge efficiency.

[a]College of Materials and Chemistry, Southwest University of Science and Technology, Mianyang, Sichuan, 621010, China. E-mail: huojichuan@163.com

[b]School of Chemistry and Chemical Engineering, Mianyang Techers' College, Mianyang, Sichuan, 621000, China. E-mail: liushuxin88@126.com

† Electronic supplementary information (ESI) available. See DOI: https://doi.org/10.1039/d5ra00107b

In recent years, sodium-ion batteries have attracted more and more attention due to their low cost and abundant resource advantages, especially cathode materials. The cathode materials mainly include layered oxide, Prussian blue and polyanionic compounds. Among these promising cathode materials, $FePO_4$ has become a research hotspot due to its simple preparation process, high structural stability, high safety, and one-dimensional Na^+ channe.[9–14] Although the $FePO_4$ cathode material has many advantages, its low ionic and electronic conductivity limits its application.[15]

Many methods have been tried to improve the electrochemical performance of $FePO_4$, including phase structure controlling, nanocrystallization and adding conductive agents, *etc.* The crystal phases of $FePO_4$ are mainly amorphous, hexagonal, monoclinic, and orthogonal. Heterosite $FePO_4$, as one of the orthogonal phases, is a metastable structure that cannot be directly prepared but is obtained by selective delithiation in $LiFePO_4$.[16] Most $FePO_4$ crystal phases can be obtained by hydrothermal or direct precipitation, but the particle size is usually in the micron scale.[17,18] To get a smaller particle size or nanocrystallization of $FePO_4$, ball milling is the key technique, and to enhance the ionic and electronic conductivity, conductive agents were usually added, including graphene, carbon nanotubes, carbon black, *etc.* Wang *et al.*[19] directly synthesized nanostructured amorphous $FePO_4$–carbon nanotube (CNT) composites with high purity $FePO_4$/C ratio controllable, the particles were refined to about 20 nm by ball milling, and showed a discharge specific capacity of 175.8 mA h g^{-1}. However, the preparation process becomes more complicated and has higher energy consumption because of the implementation of the ball milling, so a new and simple method for nanoscale $FePO_4$/C cathode materials with excellent performance is urgent.

In this work, different phase compositions, microstructures, and nano-sized $FePO_4 \cdot 2H_2O$/C and $FePO_4$/C cathode materials were prepared by ultrasonic-assisting technique with carbon black preoxidation technique. The particle size reached about 50 nm and the carbon black was evenly distributed. Meanwhile, it showed excellent electrochemical performance.

2 Materials and methods

2.1 Materials preparation

The amorphous $FePO_4 \cdot 2H_2O$/C was prepared by ultrasonic-assisted precipitating with carbon black preoxidation technique. Firstly, carbon black was oxidized in an oil bath at 80 °C for 5 h by H_2O_2 and oxidized carbon black with strong hydrophilicity was obtained, next, the oxidized carbon black (5% wt) was dispersed into $NH_4H_2PO_4$ (1 M, 60 ml) solution under strongly stirring, and then the $NH_4H_2PO_4$/oxidized carbon black solution was slowly dropped into $Fe(NO_3)_3 \cdot 9H_2O$ (1 M, 60 ml) solution to obtain a mixed solution. The mixed solution was heated to 80 °C in the mechanical-ultrasonic assisted instrument with ultrasonic power 300 W and stirring speed 300 rpm, and an appropriate amount of $NH_4 \cdot H_2O$ was slowly dripped to adjust pH, then the reaction was continued for 4 h and stand for 1 h. Finally, the amorphous $FePO_4 \cdot 2H_2O$/C was obtained. The preparation mechanism is shown in Fig. 1.

Other four kinds of cathode materials were prepared by further treatment of amorphous $FePO_4 \cdot 2H_2O$/C: (1) amorphous $FePO_4 \cdot 2H_2O$/C was calcined at different temperature in a nitrogen atmosphere for a certain time, the amorphous and hexagonal $FePO_4$/C without crystal water were separately obtained. (2) $FePO_4 \cdot 2H_2O$/C was dispersed in 5 mol L^{-1} H_3PO_4 solution, then heated and aged at different temperature in the closed reactor for different time, the monoclinic $FePO_4 \cdot 2H_2O$/C and orthogonal/monoclinic $FePO_4$/C $\cdot 2H_2O$ were separately obtained.

2.2 Materials characterization

X-ray diffractometer (XRD) was used to collect the diffraction pattern of the powder to obtain the crystal structure information. The microstructure of the samples was measured by field emission scanning electron microscopy (SEM) and high resolution transmission electron microscopy (HRTEM). The stretching vibration of carbon materials and main functional groups was analyzed using Raman spectroscopy. The particle size and specific surface area of the samples were analyzed by nitrogen adsorption/desorption testing.
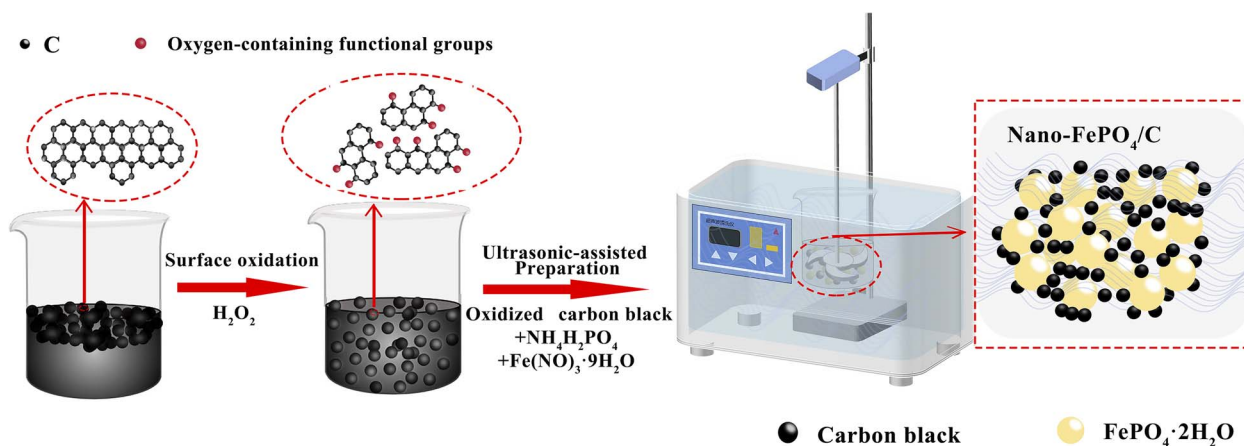

Fig. 1 Preparation mechanism diagram.

2.3 Battery assembling and electrochemical measurements

The active material was mixed with conductive agent (Super P) and binder (PVDF) according to the mass ratio of 8 : 1 : 1 into a uniform slurry, coated on aluminum foil, and baked in a vacuum drying oven at 80 °C for 20 h. After that, the positive electrode sheet required to assemble the half battery was obtained. The active material was used as the positive electrode, the sodium sheet as negative electrode, the electrolyte was 1 mol L^{-1} $NaPF_6$ (EC : DEC : EMC = 1 : 1 : 1 vol%) solution, and the separator was glass fiber (GF/D Whatman).

The constant current charge–discharge and cycle performance of the half-cell were tested by the LAND C2001A test system, the test voltage range was 1.5–4.5 V ($vs.$ Na/Na$^+$), and the charge–discharge current density was 0.1C, which defined 1C = 178 mA g^{-1}. The electrochemical impedance spectroscopy (EIS) was employed using a CHI660E electrochemical workstation over the frequency range from 0.01 to 100 kHz with an amplitude of 5 mV. The cyclic voltammetry of the half-cell was tested using an electrochemical workstation (CHI660E) at 0.1 mV s^{-1}.

3 Results and discussion

3.1 Characterization of materials

To analyze the phase structure and the amount of crystal water in the initial sample without aging and calcining, the XRD, TGA, DTG and DTA of the sample were tested. Fig. 2 shows XRD patterns of the initial sample, and its calcined sample. As can be seen from the figure, the XRD diffraction pattern of the initial sample only has a wide dispersion peak at about 25°, which is an amorphous structure, and its phase composition (including the phase of carbon) cannot be determined. To further determine the composition of the initial sample, the sample was calcined at 600 °C, and its diffraction pattern had strong diffraction peaks at 20.3°, 25.8°, 37.9°, $etc.$, which were found to be consistent with quartz-type iron phosphate (COD number: 96-901-2513) standard card has a high degree of coincidence, indicating that the main

Fig. 2 XRD patterns of the initial sample and its calcined sample.

phase of the initial sample prepared by ultrasonic assisted precipitation is iron phosphate. Meanwhile, thermal analysis was performed on the initial sample to further determine the crystal water content of the synthesized iron phosphate by precipitation.

Fig. 3 shows the thermal analysis curves of the initial sample at a heating rate of 10 °C min^{-1}. It can be seen from the TGA curve (Fig. 3a) that the quality of the sample begins to decline at about 40 °C until 500 °C, the weight of the sample is reduced by 23.95%. Combined with the analysis of the DTG curve, it can be found that the weight loss rate of the sample is the highest at 125 °C, followed by 255 °C, corresponding to the wide endothermic peak of the DTA curve (Fig. 3b) around 125 °C, it is speculated that the decomposition of crystal water and adsorbed water occurs in this temperature range. And after 500 °C, the TGA/DTG curves remain level, and the DTA curve is smooth and no difference. No significant mass loss or other physical/chemical reactions occurred in the sample, indicating that the crystal water and adsorbed water were completely removed. According to thermal analysis, the weight percentage of the dehydrated sample is 76.05%, and the sample contains 5% carbon. By calculating the actual weight percentage of the dehydrated sample is 74.79%, and according to formula (1), the number of crystal water is 2.83. Since the sample contains part of adsorbed water, there should be two crystal water. Therefore, it can be concluded that the initial sample prepared in this experiment is amorphous $FePO_4 \cdot 2H_2O$/C cathode material.

$$X = \frac{M_1(1 - \omega)}{\omega M_2} \tag{1}$$

where M_1 is the molar mass of $FePO_4$ (151 g mol^{-1}), M_2 is the molar mass of H_2O (18 g mol^{-1}), X is the number of crystal water, ω is the percentage of the weight of the sample after dehydration.

In addition to determining the amount of crystal water in the sample, it can also be found through the thermal analysis that there are exothermic peaks in the DTA curve at about 520 °C and 556.6 °C, while the corresponding TGA/DTG curve does not change significantly. It is inferred that the crystal transformation of iron phosphate from amorphous to quartz type occurs at this time.

To get different phase structures $FePO_4 \cdot 2H_2O$/C, the amorphous $FePO_4 \cdot 2H_2O$/C was aged at different temperature in the closed reactor for different time. Fig. 4a shows the XRD patterns of aged samples. First of all, we know that the $FePO_4 \cdot 2H_2O$/C without aging is an amorphous structure, and with the increase of aging temperature, the amorphous structure gradually transforms into a crystal structure. Further analysis find that the samples aged at 50 °C are amorphous structures. When the aging temperature is 70 °C and the time is 2 h, some weaker diffraction peaks appear at around 19°, 20.5°, 24.5° and 32°, which belong to monoclinic structure (COD no. 96-431-8789), and the aging time is extended to 4 h, these diffraction peaks gradually increase. When the aging temperature is 90 °C and the time is 2 h or 4 h, the phase structure of samples still remains in monoclinic structure. When the temperature rises further, some new diffraction peaks appear at around 16°, 22° and 29° which belong to orthogonal structure (COD no. 96-901-
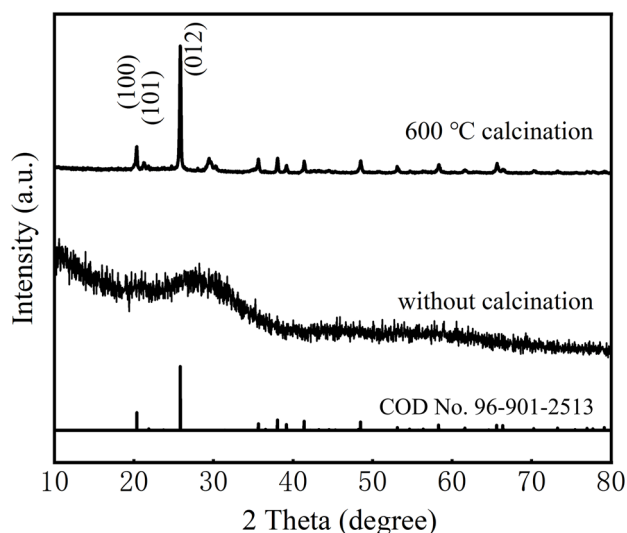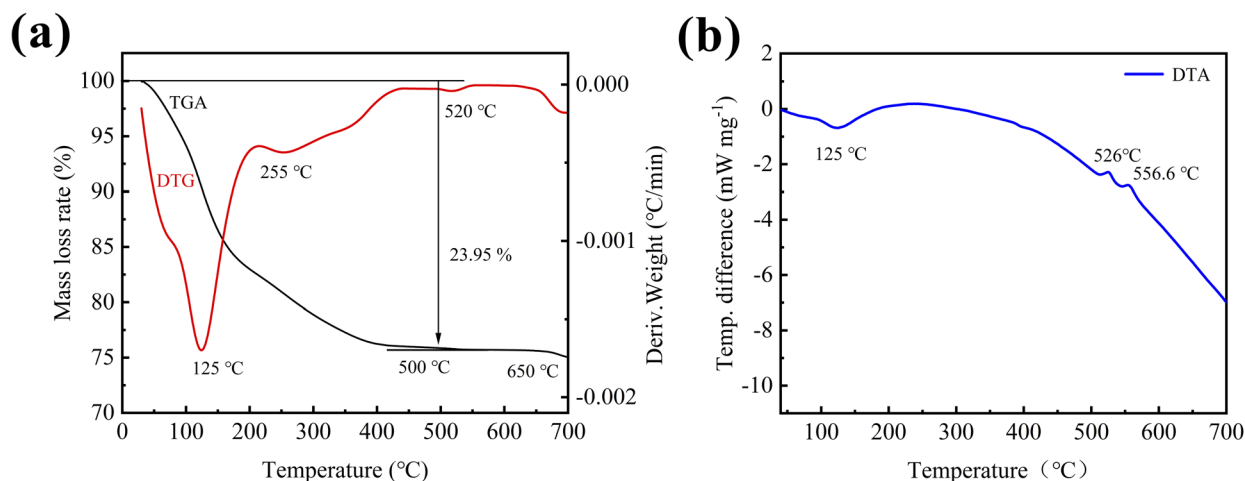
Fig. 3 TGA/DTG (a) and DTA (b) curves of the initial sample.

0008), but the diffraction peaks of monoclinic structure do not diminish, it indicates that the orthogonal structure transforms from amorphous structure, not monoclinic structure, and the transform process is slower and more difficult than monoclinic structure. All of the samples, including amorphous, monoclinic and monoclinic/orthogonal structures contain crystal water.
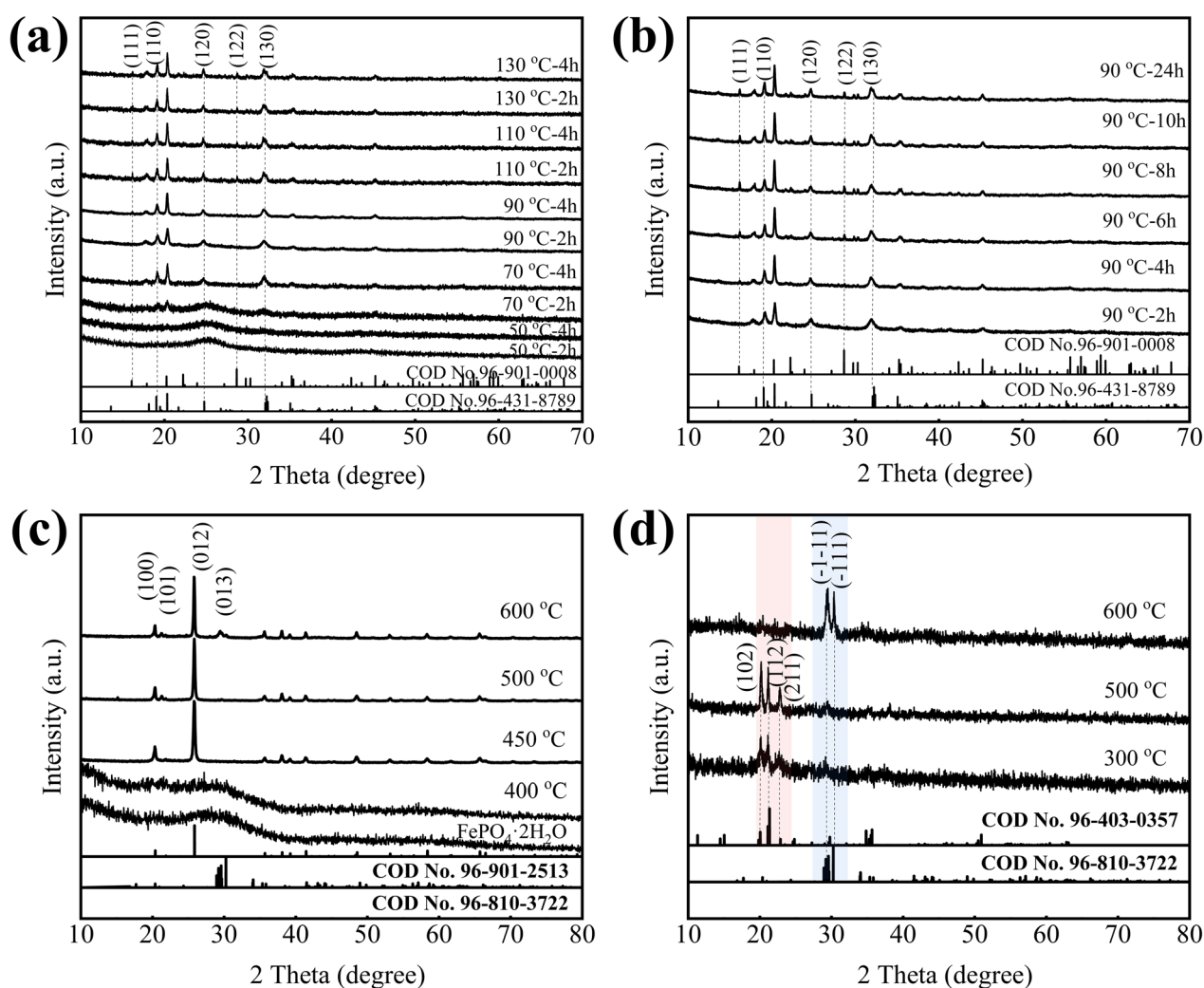

Fig. 4 The XRD pattern of samples aged at different temperatures for a-FPH/C (a), aged at 90 °C in different time for a-FPH/C (b), calcined at different temperature for a-FPH/C (c), and calcined at different temperature for om-FPH/C (d).

In order to study the phase transform process of the $FePO_4 \cdot 2H_2O/C$, amorphous $FePO_4 \cdot 2H_2O/C$ was aged at 90 °C for different time. From Fig. 4b, it can be found that the orthogonal diffraction peaks of $FePO_4 \cdot 2H_2O$ (COD no. 96-901-0008) increase gradually with aging time, and the monoclinic diffraction peaks did not diminish, the orthogonal and monoclinic structure coexist.

To obtain different phase structures of $FePO_4/C$ without crystal water, the amorphous $FePO_4 \cdot 2H_2O/C$ was calcined at 400 °C, 450 °C, 500 °C and 600 °C in a nitrogen atmosphere for 2 h. Fig. 4c is the XRD patterns of $FePO_4/C$ prepared at different calcination temperature, it can be found that the calcination temperature has a major impact on the phase structure of $FePO_4$, when the calcination temperature is 400 °C, the phase structure of $FePO_4$ is amorphous structure, which indicates that when $FePO_4 \cdot 2H_2O/C$ is calcined below 400 °C, the phase structure is amorphous structure. With the calcination temperature rising, a rise of only 50 °C, the amorphous structure transforms into hexagonal structure, it has a high matching degree with the diffraction peaks of hexagonal $FePO_4$ indexed in the standard card (COD no. 96-901-2513), and there are no other peaks, indicating that the $FePO_4$ crystal can be synthesized at 450 °C. As temperature calcination continues to rise, the phase structure does not change. When the temperature rises to 600 °C, the anorthic $Fe_2P_2O_7$ phase (COD no. 96-810-3722) appears at nearly 30°, which indicates that Fe^{3+} is reduced to Fe^{2+} by carbon black, the reaction mechanism could be: $2FePO_4 + C = Fe_2P_2O_7 + CO\uparrow$, $2FePO_4 + CO = Fe_2P_2O_7 + CO_2\uparrow$. The above analysis indicates that the amorphous and hexagonal $FePO_4/C$ without crystal water can be only obtained by calcining amorphous $FePO_4 \cdot 2H_2O/C$, and other phase structure $FePO_4/C$ without crystal water cannot be obtained.

To obtain monoclinic or orthogonal $FePO_4/C$ without crystal water, the monoclinic/orthogonal $FePO_4 \cdot 2H_2O/C$ were calcined at 300 °C, 500 °C, 600 °C for 8 h, the XRD patterns shown in Fig. 4d. When the calcination temperature is 300 °C and 500 °C, the main phase is the orthorhombic $Fe_3P_4O_{14}$ (COD no. 96-403-0357) and little anorthic $Fe_2P_2O_7$ (COD no. 96-810-3722), it indicates that some of Fe^{3+} are reduced. When the calcination temperature is 600 °C, the main phase is the anorthic $Fe_2P_2O_7$ indicating that most of Fe^{3+} are reduced, this can be attributed to the fact that Fe^{3+} is reduced by carbon black. These experiments indicate that the monoclinic or orthogonal $FePO_4/C$ without crystal water cannot be synthesized by calcination due to the presence of carbon black.

Based on the above analysis, the samples of the initial amorphous $FePO_4 \cdot 2H_2O/C$ without aging and calcining (a-FPH/C), monoclinic $FePO_4 \cdot 2H_2O/C$ (m-FPH/C) and orthogonal/monoclinic $FePO_4 \cdot 2H_2O/C$ (om-FPH/C) prepared by aging a-FPH/C at 90 °C for 2 h and 8 h, and amorphous $FePO_4/C$ (a-FP/C) and hexagonal $FePO_4/C$ (h-FP/C) prepared by calcining a-FPH/C at 400 °C for 2 h and at 600 °C for 2 h are used as research objects.

Fig. 5 is the Raman spectrum of the samples, and the characteristic Raman peaks belonging to carbon can be detected. The G band corresponds to the E_{2g} phonon at the Brillouin zone center, which indicates sp^2 hybridized carbon atoms arranged
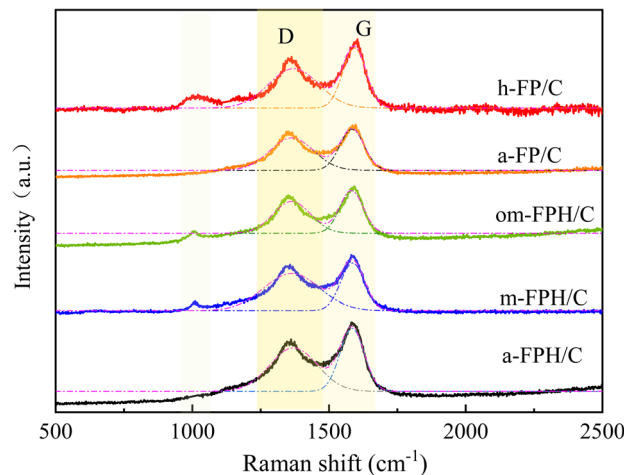

Fig. 5 Raman spectrum of the samples.

in a graphitic structure, the D band arises from defects and disorder within this structure. By comparing the peak areas of the G band and D band, the large ratio of peak area (Table 1) of the G band relative to the D band exhibits a high degree of graphitization, and highly graphitized carbon materials are known to possess enhanced electrical conductivity.[16,20–26] Meanwhile, all of the ratios of I_G/I_D are basically equal, which indicates that the oxidizing, calcining and aging processes do no effect carbon black. Furthermore, it can be observed that a broad band centered at 1064 cm^{-1} is present in the Raman spectrum of m-FPH/C, om-FPH/C and h-FP/C, it is the characteristic of iron being tetrahedrally coordinated attributed to the formation of tetrahedrally-coordinated iron atoms to the enhanced surface energy kinetics at lower crystallite sizes,[27–29] whereas this band is not present in a-FPH/C and a-FP/C, further demonstrating their amorphous structure.

Fig. 6 is the SEM and TEM of the samples. In the figures, the amorphous $FePO_4 \cdot 2H_2O/C$ (a-FPH/C) particles are globular and uniform in size, about 50 nm (Fig. 6b). The monoclinic m-FPH/C and orthogonal/monoclinic om-FPH/C are flake (Fig. 6c–f), and there are some small flocculent particles in these samples, they should be carbon black, and the flake of m-FPH/C is bigger than om-FPH/C, the thickness of flakes is about 20 nm. Both amorphous a-FP/C and hexagonal h-FP/C have near-spherical shapes (Fig. 6g–j), the particle dispersion is more uniform, and the particle size is about 50 nm (Fig. 6h and j), and in contrast to the a-FPH/C, the calcination temperature and phase changing are almost no effects on particles size. At the same time, because the samples of a-FPH/C, a-FP/C and h-FP/C are spherical and the particle size is small, carbon black is not easy to identify.

In order to further prove the existence of carbon and the distribution of each element, elemental analysis of amorphous $FePO_4 \cdot 2H_2O/C$ (a-FPH/C) is carried out by energy dispersion spectroscopy (EDS), and the results are shown in Fig. 7. As shown in the figures, all elements are evenly distributed, the molar ratio of Fe/P is close to 1 : 1, and the content of carbon black is 5 wt%. In summary, the nano-size $FePO_4 \cdot 2H_2O/C$ cathode materials with uniform particle distribution were

Table 1 Raman spectra peak position and I_G/I_D ratio of the samples

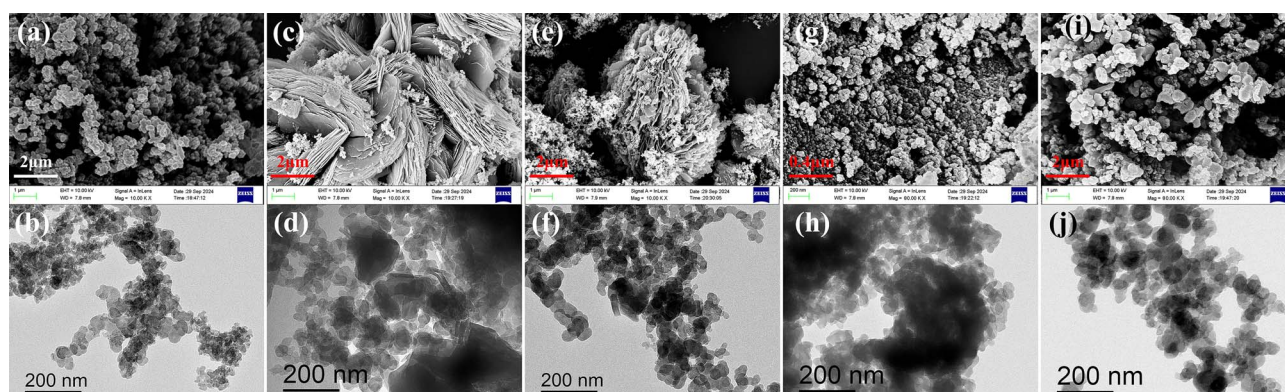| Samples	Peak D		Peak G		I_G/I_D
	Area	Position (cm^{-1})	Area	Position (cm^{-1})	
a-FPH/C	247 988.48	1370.1	182 993.54	1584.2	0.738
m-FPH/C	236 596.62	1370.6	166 715.26	1592.9	0.705
om-FPH/C	203 405.07	1363.4	145 787.86	1586.3	0.718
a-FP/C	170 298.07	1363.4	120 221.00	1584.2	0.706
h-FP/C	161 927.08	1363.9	119 317.61	1582.3	0.737

Fig. 6 SEM and TEM of samples. (a) and (b) are SEM and TEM of a-FPH/C, (c) and (d) are SEM and TEM of m-FPH/C, (e) and (f) are SEM and TEM of om-FPH/C, (g) and (h) are SEM and TEM of a-FP/C, (i) and (j) are SEM and TEM of h-FP/C.
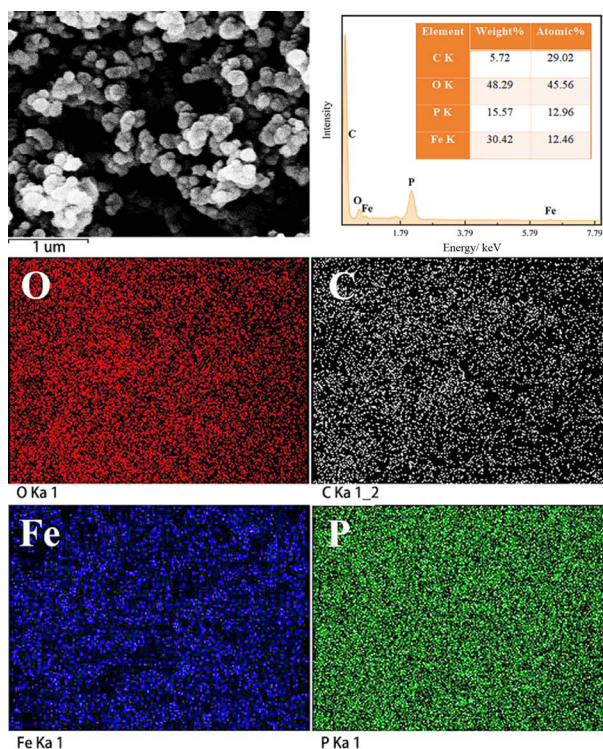

Fig. 7 Element distribution mappings of a-FPH/C.

successfully prepared by ultrasonic-assisted preparation, and carbon black to form a conducting network structure in samples.

Fig. 8 shows the N$_2$ adsorption–desorption isotherm and pore size distribution of the samples. The adsorption–desorption curves of the five samples display IV-type isotherms with H1 hysteresis loop, H3 hysteresis loop, and H4 hysteresis loop, H1 hysteresis loop, H3 hysteresis loop, respectively. The type of hysteresis loop corresponds to the specific pore structure information. Among them, H1 is a uniform pore model, which can be considered as a cylindrical pore, while H3 and H4 have a large adsorption amount under high pressure, which can be considered as a narrow pore formed by the accumulation of flake particles or a large pore formed by the accumulation of big particles. At the same time, the pore size distribution also further verifies that the pore of samples is mainly mesoporous. Table 2 shows the specific surface area and pore size of the samples. It can be seen that the amorphous structure a-FPH/C and a-FP/C have a larger specific surface area of 85.021 m^2 g^{-1} and 70.289 m^2 g^{-1}. This is because the calcining changes particle size and porosity, and heating and aging change particle size and shape.

3.2 Electrochemical performance analysis

Fig. 9 shows the electrochemical properties of samples prepared by ultrasonic-assisted preparation. Fig. 9a illustrates the Nyquist plot of samples, all of the curves comprise a straight line at low frequencies and a semicircle at high to medium frequencies, where the linear portion signifies sodium ion diffusion within the electrode, while the semicircular part denotes charge transfer occurring on the cathode surface.[30,31] The corresponding equivalent circuit model is presented in
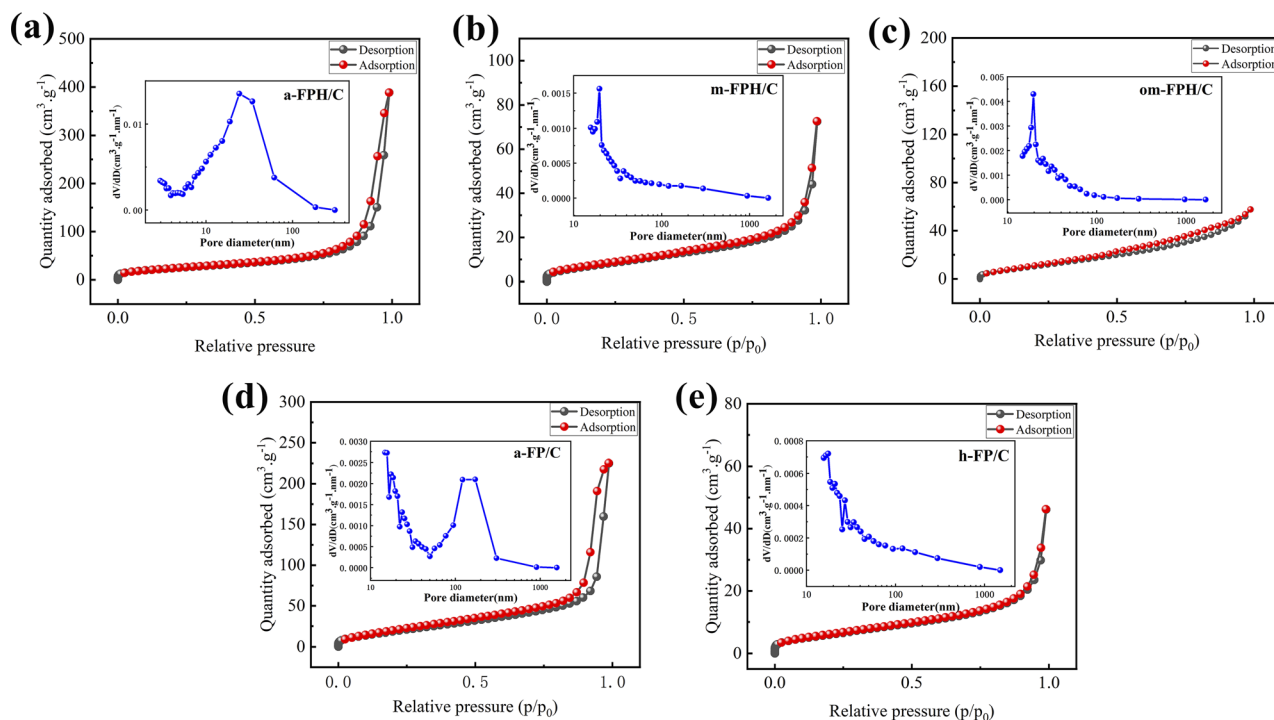
Paper

RSC Advances

Fig. 8 N$_2$ adsorption–desorption isotherm and pore size distribution of a-FPH/C (a), m-FPH/C (b), om-FPH/C (c), a-FP/C (d), and h-FP/C (e).

Table 2 Specific surface area and pore size of the samples

Sample	S_{BET} (m^2 g^{-1})	Pore volume (cm^3 g^{-1})	Average pore size (nm)
a-FPH/C	85.021	0.598	24.314
m-FPH/C	22.303	0.106	19.649
om-FPH/C	46.255	0.086	19.640
a-FP/C	70.289	0.341	14.845
h-FP/C	14.579	0.066	17.513

Fig. 9a, the charge transfer resistance (R_{ct}) values of a-FPH/C, m-FPH/C, om-FPH/C, a-FP/C and h-FP/C after fitting are 205, 833, 618, 139, 1020 Ω, respectively. It can be found that the R_{ct} of a-FP/C is much lower than that of other phase structures, indicating that the amorphous FePO$_4$/C materials have better electronic conductivity. The reason is that a larger specific surface area of a-FP/C improves the point contact between the active particles and the carbon black, which is conducive to bipolar diffusion,[18] and the isotropic and defectless properties of amorphous FePO$_4$ provides a large number of continuous channels for Na$^+$.[32,33]

Since there is a good linear relationship between the resistance (Z') and the angular velocity ($\omega^{-1/2}$) (Fig. 9b), the specific Na$^+$ diffusion rate (D_{Na^+}) can be calculated according to this relationship. The sodium diffusion coefficient in Fig. 9c is calculated using formula (2).[34–38]

$$D_{Na^+} = \frac{R^2 T^2}{2A^2 n^4 F^4 C^2 \delta^2} \quad (2)$$

where σ is the Warburg factor, C is the concentration of Na$^+$ in the cathode, F is the Faraday constant, n is the number of

electrons transferred by each molecule of redox reaction, A is the surface area of the electrode, T is the corresponding absolute temperature, and R is the universal gas constant.

The calculated results (Fig. 9c) show that the diffusion coefficients of Na$^+$ are 2.34×10^{-16}, 2.24×10^{-16}, 2.40×10^{-16}, 2.71×10^{-16} cm^2 s^{-1} and 1.81×10^{-17} cm^2 s^{-1} for a-FPH/C, m-FPH/C, om-FPH/C, a-FP/C, and h-FP/C, respectively. The maximum Na$^+$ diffusion coefficient of a-FP/C further proves that the amorphous structure without crystal water is favorable to the electrochemical performance. Fig. 9d is the cyclic voltammetry of samples at a scan rate of 0.1 mV s^{-1} in the voltage range of 1.5–4.5 V at room temperature, one pair of oxidation–reduction current peaks of Fe^{3+}/Fe^{2+} can be seen located near 3.1 V, the wide oxidation–reduction peak proves that the sodiation/desodiation process is a continuous one-phase oxidation–reduction reaction. Meanwhile, a-FP/C has the smallest potential difference, indicating the lowest degree of electrode polarization, which also shows that the amorphous structure, nano-sized spherical particles, large specific surface area, spatial network structure of carbon black enhance the sodiation/desodiation kinetics of cathode material.

Fig. 10a is the initial charge–discharge curves of samples at 0.1C at room temperature. The discharge specific capacity of a-FPH/C, m-FPH/C, om-FPH/C, a-FP/C and h-FP/C is 124.1, 94.9, 114.6, 149.8, 68.1 mA h g^{-1}, respectively. From the comparison, whether or not containing crystal water, the amorphous structure materials have higher discharge specific capacity, the reason is the amorphous structure can provide more Na$^+$ transport channels, meanwhile, the amorphous structure has a larger specific surface area, which means that there are more
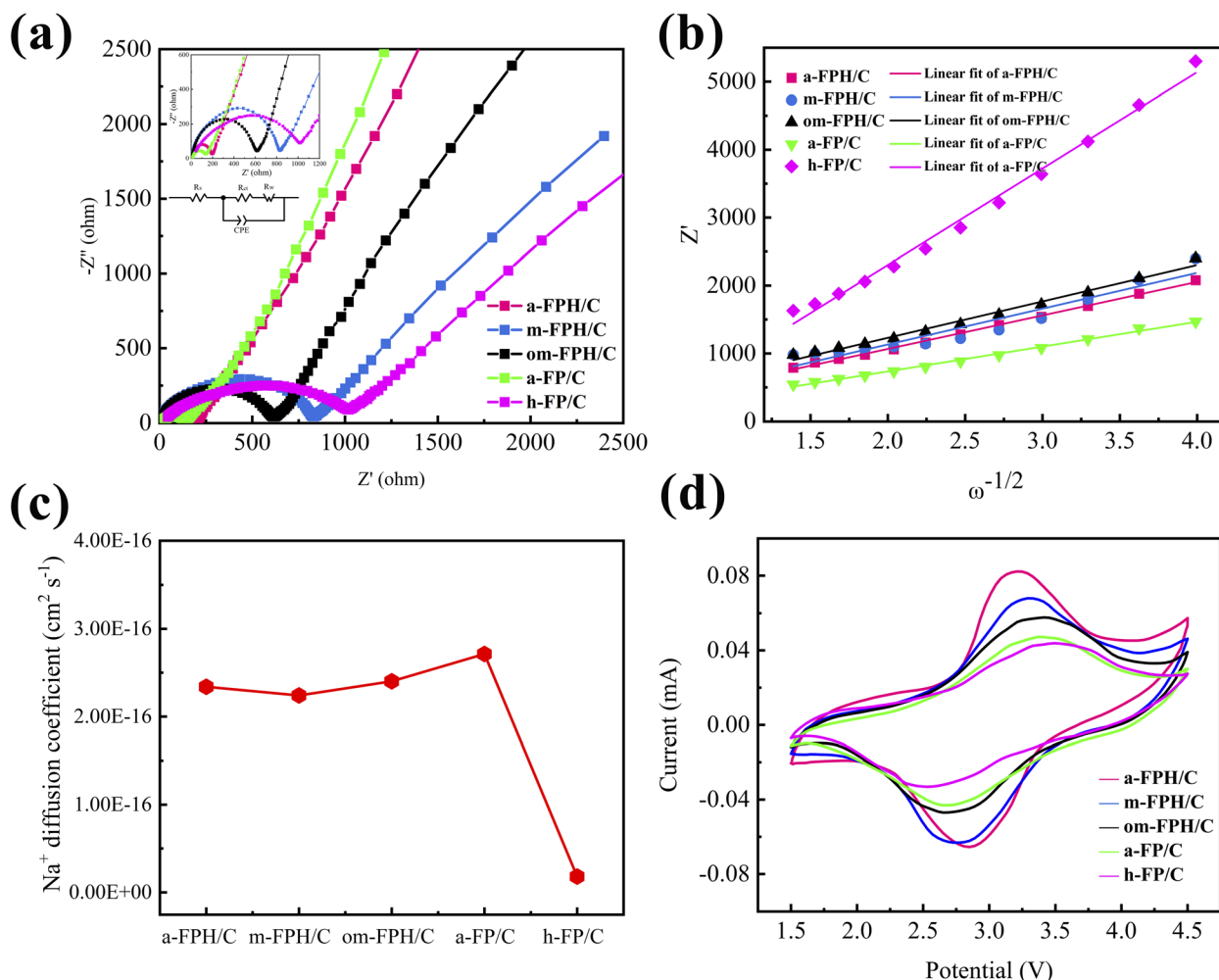
Fig. 9 Electrochemical impedance spectroscopy of samples (a). The relationship between the resistance (Z') and the inverse square root of the angular speed (b). The slope (δ) and Na$^+$ diffusion coefficient of samples (c). Cyclic voltammetry of samples at a scan rate of 0.1 mV s^{-1} in the voltage range of 1.5–4.5 V at room temperature (d).
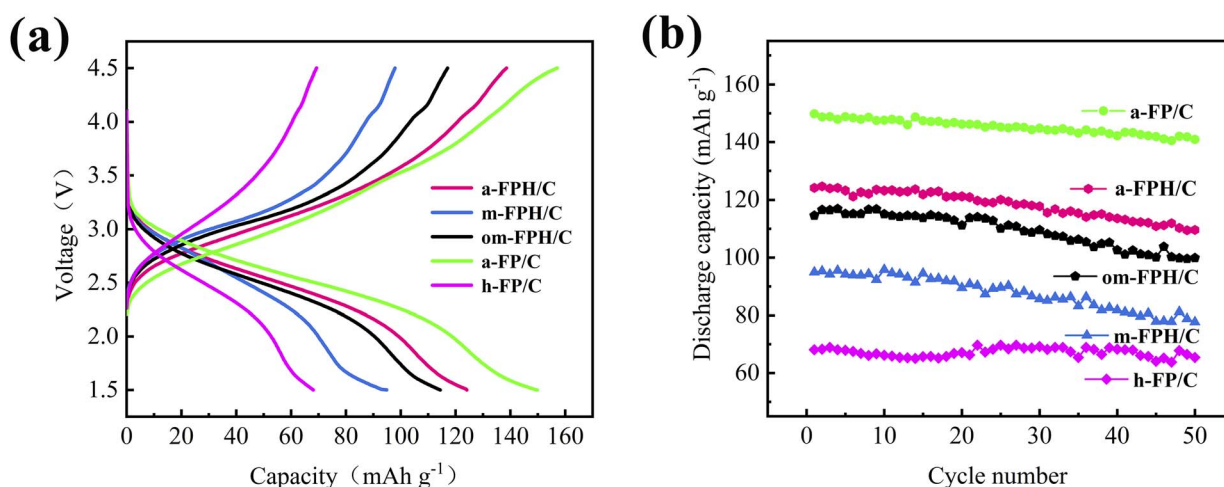

Fig. 10 Charge–discharge curves (a) of samples and cycling performance (b) of samples at 0.1C at room temperature.

contact surfaces with conductive carbon black and electrolytes. Moreover, the amorphous a-FP/C without crystal water has the maximum discharge specific capacity, this may be the crystal water may hinder Na$^+$ transport channel and may react with electrolyte, reducing the reversibility of sodiation/desodiation during charge and discharge. In the calcining amorphous

$FePO_4 \cdot 2H_2O$/C process, with the increase of calcination temperature, the amorphous structure is transformed into hexagonal structure which has high stability, but the more stable structure usually has lower electrochemical activity,[39] so it has the minimum discharge specific capacity. Comparing m-FPH/C and om-FPH/C, the discharge specific capacity of om-FPH/C containing partially orthogonal structure is higher than m-FPH/C, it shows that orthogonal structure has better electrochemical performance than monoclinic structure. Fig. 10b is the cycling performance of samples at 0.1C at room temperature, the cycling performance of a-FP/C is excellent, and with the increase in the number of cycles, the capacity retention rate is 94.06%. It also has been found that the discharge specific capacity of the samples with crystal water (a-FPH/C, m-FPH/C and om-FPH/C) decreases seriously with the increase of the number of cycles, it further shows that the crystal water will be detrimental to charge and discharge process. Based on the above experimental results, compared with the existing literature,[11,14,15,25,40] this work adopts a relatively simple experimental process to synthesize amorphous structural $FePO_4$/C cathode materials, and obtains similar or better experimental results.

4 Conclusion

To study the electrochemical performance of $FePO_4$ with different crystal phases, ultrasonic-assisting technique was applied to the precipitation reaction process of $FePO_4$/C for sodium ion battery, and the different phase composition and microstructure cathode materials including amorphous and hexagonal structure $FePO_4$/C without crystal water, and the amorphous, monoclinic and orthogonal/monoclinic $FePO_4$/C with crystal water were prepared. The peroxidation for carbon black and ultrasonic application in the preparation process obtain the high dispersity and ultrafining cathode materials. Furthermore, the peroxidation doesn't change the structure of carbon black. Because of the highly nano-sized particles, higher specific surface area, and a continuous and uniform carbon spatial network structure, all the samples showed a certain improvement in electrochemical performance, especially a-FP/C. Moreover, the amorphous structure can provide more Na^+ transport channels than other phase structures, and the crystal water was removed by calcining which is more conducive to ion transport, so, a-FP/C shows an excellent discharge specific capacity, the maximum Na^+ diffusion coefficient, the minimum charge transfer resistance and good cycle performance. This work provides a new insight into the preparation of the enhanced electrochemical performance for $FePO_4$/C, and is helpful in developing new battery materials through the ultrasonic technique.

Data availability

Data will be made available on request.

Author contributions

Chunmei Tang: methodology, investigation, writing – original draft. Wei Ma: data curation. Jichuan Huo: conceptualization,

supervision. Shuxin Liu: writing – review, conceptualization, resources & editing.

Conflicts of interest

There are no conflicts to declare.

Acknowledgements

References

1 C. Zhang, S. Chou, Z. Guo and S. Dou, *Adv. Funct. Mater.*, 2024, **34**, 2308001.

2 T. Dong, K. L. Ng, Y. Wang, O. Voznyy and G. Azimi, *Adv. Energy Mater.*, 2021, **11**, 2100077.

3 Z. Xiao, F. Xia, L. Xu, X. Wang, J. Meng, H. Wang, X. Zhang, L. Geng, J. Wu and L. Mai, *Adv. Funct. Mater.*, 2022, **32**, 2108244.

4 D. Wang, Y. Wu, J. Lv, R. Wang and S. Xu, *Colloids Surf., A*, 2019, **583**, 123957.

5 L. Zhang, J. Liu, Y. Zhai, S. Zhang, W. Wang, G. Li, L. Sun, H. Li, S. Qi, S. Chen, R. Wang, Q. Ma, J. Just and C. Zhang, *Adv. Mater.*, 2024, **36**, 2313835.

6 X. Zhang, R. Wang, Z. Liu, Q. Ma, H. Li, Y. Liu, J. Hao, S. Zhang, J. Mao and C. Zhang, *Adv. Energy Mater.*, 2024, **14**, 2400314.

7 P. Hu, T. Zhu, C. Cai, X. Wang, L. Zhang, L. Mai and L. Zhou, *Angew. Chem., Int. Ed.*, 2023, **62**, e202219304.

8 C. Wang, Q. Yao, M. Wang, C. Zheng, N. Wang, Z. Bai, J. Yang, S. Dou and H. Liu, *Adv. Funct. Mater.*, 2024, **34**, 2301996.

9 X. Zhao, S. Yang, X. Song, Y. Wang, H. Zhang, M. Li and Y. Wang, *Adv. Sci.*, 2024, **11**, 2405176.

10 Y. Wang, Z. Feng, D. Laul, W. Zhu, M. Provencher, M. L. Trudeau, A. Guerfi and K. Zaghib, *J. Power Sources*, 2018, **374**, 211–216.

11 W. Wang, S. Wang, H. Jiao, P. Zhan and S. Jiao, *Phys. Chem. Chem. Phys.*, 2015, **17**, 4551–4557.

12 Q. Fan, L. Lei, G. Yin, Y. Chen and Y. Sun, *Electrochem. Commun.*, 2014, **38**, 120–123.

13 M. R. Cerón, M. Izquierdo, N. Alegret, J. A. Valdez, A. Rodríguez-Fortea, M. M. Olmstead, A. L. Balch, J. M. Poblet and L. Echegoyen, *Chem. Commun.*, 2016, **52**, 64–67.

14 S.-Y. Duan, J.-Y. Piao, T.-Q. Zhang, Y.-G. Sun, X.-C. Liu, A.-M. Cao and L.-J. Wan, *NPG Asia Mater.*, 2017, **9**, e414.

15 Y. Wang, M. Deng, X. Zhang, J. Zhang, Y. Sui, K. Sun, K. Rao and L. Wu, *J. Colloid Interface Sci.*, 2024, **661**, 23–32.

16 A. Banday, R. Shahid, M. Cupta and S. Murugavel, *RSC Adv.*, 2023, **13**, 18332.

17 J. Ma, L. Wang, F. Yu and X. Dai, *Chem. Eng. J.*, 2019, **370**, 938–943.

18 C. Li, X. Wang, J. Li and H. Wang, *Chem. Commun.*, 2018, **54**, 4349–4352.

19 Z. Wang and Y. Lu, *ACS Omega*, 2019, **4**, 14790–14799.

20 K. He, Z. Xu, X. Zhang, Q. Li and F. Wang, *Spectrochim. Acta, Part A*, 2023, **289**, 122249.

21 N. Hassanzadeh, S. K. Sadrnezhaad and G. Chen, *Electrochim. Acta*, 2016, **208**, 188–194.

22 I. P. Vali, B. S. Anusha, M. Pruthvija, S. Savitha, S. Ravindra, M. Nagaveni, P. S. Poojitha and N. Swathi, *Mater. Chem. Phys.*, 2024, **318**, 129240.

23 M. Shi, D. Bao, S. Li, B. Wulan, J. Yan and Q. Jiang, *Adv. Energy Mater.*, 2018, **8**, 1800124.

24 C. M. Burba, J. M. Palmer and B. S. Holinsworth, *J. Raman Spectrosc.*, 2009, **40**, 225–228.

25 Z. Wang, J. Liu, X. Zhang, Y. Wang, D. Wang, W. Shi, H. Li, P. Zhang, J. Man and L. Liu, *J. Non-Cryst. Solids*, 2024, **634**, 122983.

26 A. Banday, R. Shahid, S. S. Meena, S. M. Yusuf and S. Murugavel, *Phys. Chem. Chem. Phys.*, 2020, **22**, 15478–15487.

27 L. Popovi, D. De Waal and J. C. A. Boeyens, *J. Raman Spectrosc.*, 2005, **36**, 2–11.

28 J. Haines, O. Cambon and S. Hull, *Z. Kristallogr. – Cryst. Mater.*, 2003, **218**, 193–200.

29 P. Tarte, *Solid State Ionics*, 1990, **42**, 177–196.

30 W. Lou, Y. Zhang, Y. Zhang, S. Zheng, P. Sun, X. Wang, S. Qiao, J. Li, Y. Zhang, D. Liu, M. Wenzel and J. J. Weigan, *J. Alloys Compd.*, 2021, **856**, 158148.

31 W. Wang, S. Wang, H. Jiao, P. Zhan and S. Jiao, *Phys. Chem. Chem. Phys.*, 2015, **17**, 4551–4557.

32 C. X. Guo, Y. Q. Shen, Z. L. Dong, X. D. Chen, X. W. Lou and C. M. Li, *Energy Environ. Sci.*, 2012, **5**, 6919.

33 Y. Yin, Y. Hu, P. Wu, H. Zhang and C. Cai, *Chem. Commun.*, 2012, **48**, 2137.

34 X. Ren, Z. Li, J. Cao, S. Tian, K. Zhang, J. Guo, L. Wen and G. Liang, *J. Alloys Compd.*, 2021, **867**, 158776.

35 Y. Zuo, J. Yue, Z. Ma and Z. Zuo, *J. Phys. Chem. Solids*, 2022, **160**, 110354.

36 H. Xiao, J. P. Pender, M. A. Meece-Rayle, J. P. De Souza, K. C. Klavetter, H. Ha, J. Lin, A. Heller, C. J. Ellison and C. B. Mullins, *ACS Appl. Mater. Interfaces*, 2017, **9**, 22641–22651.

37 Y. Zhang, H. Jin, H. Tu, Y. Zuo, Q. Luo, P. Li, Z. Chen, J. Jia and L. Zhang, *J. Ind. Text.*, 2023, **53**, 1–16.

38 X. Tian, Y. Zhou, X. Tu, Z. Zhang and G. Du, *J. Power Sources*, 2017, **340**, 40–50.

39 Y. Pei, C. Liu, Z. Han, Z. G. Neale, W. Qian, S. Xiong, Z. Jiang and G. Cao, *J. Power Sources*, 2019, **431**, 75–83.

40 B. Pandit, B. Fraisse, L. Stievano, L. Monconduit and M. T. Sougrati, *Electrochim. Acta*, 2022, **409**, 139997.